https://doi.org/10.5194/egusphere-2026-3677
Preprint. Discussion started: 10 July 2026

The Dissipation of Shallow Cumulus Clouds: Dynamics, Microphysics, and Environmental Signatures

Yael Arieli[1], Alexander Khain[2], Orit Altaratz[1], Ehud Gavze[2], and Ilan Koren[1]

[1]Department of Earth and Planetary Science, Weizmann Institute of Science, Rehovot, Israel
[2]Institute of Earth Science, Hebrew University, Jerusalem, Israel

Correspondence: Alexander Khain (alexander.khain@mail.huji.ac.il) and Ilan Koren (Ilan.Koren@weizmann.ac.il)

Abstract. The dissipation stage of shallow cumulus clouds remains less understood than their growth and mature stages, despite occupying a large fraction of the cloud lifetime. Here, we investigate the dissipation of isolated shallow cumulus clouds using high-resolution simulations across a range of initial cloud condensation nuclei (CCN) concentrations. We show that, while the growth stage is characterized by relatively smooth and monotonic evolution of bulk cloud properties, dissipation is marked by an overall decline accompanied by pronounced oscillations.

Dynamically, dissipation is characterized by weakening of the coherent large-scale circulations and an increasing relative contribution of small-scale turbulence. In non-precipitating polluted clouds, continued upward transport of moist air from cloud base allows lower-cloud updrafts to persist even as the upper cloud decays. In contrast, in precipitating clean clouds, rain formation strengthens downdrafts. The microphysical evolution also depends strongly on aerosol loading: clean precipitating clouds exhibit rapid depletion of small droplets and growth of large drops, whereas polluted non-precipitating clouds undergo weaker temporal changes. Dissipation also leaves a clear imprint on the cloud's surrounding environment. Enstrophy increases outside the cloud, indicating enhanced vorticity near the cloud–environment interface that extends outward through detrainment. A humid halo develops and expands around the cloud, exhibiting oscillatory behavior in both precipitating and non-precipitating cases.

Overall, our results show that shallow-cumulus dissipation is a distinct and prolonged stage involving coupled changes in cloud dynamics, microphysics, turbulence, and the near-cloud environment. Therefore, dissipation should be explicitly considered when interpreting instantaneous observations and representing shallow convection in models.

1 Introduction

Shallow trade cumuli clouds are ubiquitous over the tropical and subtropical oceans (Stevens, 2005). Despite their small horizontal scales (typically < 1 km), they play a central role in maintaining the tropical circulation and in transporting moisture, aerosols, heat, and momentum from the boundary layer and into the free troposphere (Johnson and Lin, 1997). It is common to describe the evolution of individual cumulus clouds through a life cycle of three stages: growth, maturity, and dissipation. During the last stage, their dynamical and microphysical structure changes substantially (Grinnell et al., 1996; Katzwinkel et al., 2014; Zhao and Austin, 2005a, b; Lim and Hoffmann, 2024; Witte et al., 2014; French et al., 1999). For example, mixing char-

https://doi.org/10.5194/egusphere-2026-3677
Preprint. Discussion started: 10 July 2026

acteristics can shift from predominantly homogeneous early in the life cycle toward increasingly inhomogeneous mixing later on, with inhomogeneous mixing becoming especially important during dissipation under drier and more polluted conditions (Lim and Hoffmann, 2024). Mass-flux analysis shows that cloud decay is dynamically asymmetric relative to cloud growth. Numerical simulations and observations (Grinnell et al., 1996; Zhao and Austin, 2005b) show that trade cumuli typically evolve from a growth stage with upward mass transport throughout the cloud depth, to a mature stage in which net downward mass flux develops in the upper part of the cloud, while upward transport persists at lower levels, and finally to a dissipation stage characterized by net downward mass transport across most or all of the cloud (Grinnell et al., 1996; Zhao and Austin, 2005b). Understanding this asymmetry requires accounting for the broad range of motions that contribute to cloud evolution, from small-scale turbulence to vortical and larger-scale circulations. Deviations from adiabatic behavior within clouds arise from the combined effects of convective and turbulent motions (Pinsky et al., 2021). Using wavelet filtering to separate the velocity field of a high-resolution simulation of trade cumulus into convective and turbulent components, Pinsky and Khain (2023) showed that turbulent kinetic energy reaches its largest values during the dissipation stage, when the cloud top descends toward the base of the inversion layer. Arieli et al. (2024) analyzed Lagrangian passive-tracer trajectories as a function of adiabatic fraction (AF) experienced within shallow cumulus clouds. They identified three main mixing regimes during the growing and mature stage, each associated with a distinct subset of tracer pathways: a core mixing regime associated with ascent from cloud base through the cloud core, a skin mixing regime associated with small-scale turbulence at the cloud edge, and a periphery mixing regime associated with convective-scale mixing, likely linked to toroidal circulation(Eytan et al., 2024; Khain et al., 2024). During dissipation, they identified an additional fourth regime, characterized by cloud-top entrainment followed by downdrafts. During decay, there is strong mixing of the cloud's top with its environment and intense evaporation, which drives the upper-level descent. Using a toy model of dissipating nonprecipitating cumulus, Pinsky and Khain (2020) showed that both cloud downdrafts and lateral mixing contribute to cloud dissipation, but affect different aspects of the decay. Cloud downdrafts primarily control the reduction in cloud liquid water content, whereas mixing has a stronger influence on cloud shape and cloud narrowing because it acts most efficiently near cloud edges. Because several processes act simultaneously during the late stages of cloud evolution, the dissipation phase does not simply mirror the growth phase in reverse. Instead, processes such as precipitation formation, evaporation, and entrainment jointly influence how rapidly a cloud decays. For example, increased aerosol concentration can suppress precipitation development and therefore extend cloud lifetime, but, on the other hand, it also enhances evaporation and entrainment, which may accelerate the decay of shallow clouds, so the end result is a combined effect of all processes (Jiang et al., 2006).

In practice, the traditional three-stage description of a cloud's lifetime is often difficult to apply because shallow Cumulus clouds often evolve through pulse-like events. Observational studies and simulations indicate that many cumuli develop through a sequence of buoyancy pulses (or successive thermals) rather than a single coherent updraft (Grinnell et al., 1996; French et al., 1999; Heus et al., 2009; Scorer and Ludlam, 1953). According to Heus et al. (2009), these pulses are largely self-sustained by the cloud dynamics. Moist air from the subcloud layer is supplied continuously into a weakly buoyant transition layer just above cloud base (the CIN layer). Once air parcels rise above this layer, they accelerate upward due to buoyancy and form a coherent pulse. The upward acceleration induces horizontal convergence in the lower cloud region and entrainment of environmental

https://doi.org/10.5194/egusphere-2026-3677
Preprint. Discussion started: 10 July 2026

air into the cloud. This entrainment progressively dilutes the rising pulse, weakens its buoyancy, and eventually causes its detachment from the source region (see Fig. 17 in (Heus et al., 2009)). This transition layer above cloud base, therefore, acts as a buffer that steadily releases moist air upward, enabling the formation of subsequent pulses. In this interpretation, pulsating growth is a property of the cloud itself, and the pulses are independent of the subcloud layer. A pulse framework usefully describes repeated growth episodes, but it also implies that different parts of the same cloud can be in different 'stages' at the same time, for example, renewed ascent near cloud base can coexist with decay aloft, challenging any unique, single-valued definition of cloud age or lifecycle phase(Witte et al., 2014).

Witte et al. (2014) used large-eddy simulations of trade cumulus to propose a physically motivated "cloud clock" based on the normalized total-water mixing ratio, r_t^*, which generally decreases through the cloud lifetime as entrainment mixes drier environmental air into the cloud. Combined with buoyancy, this quantity can help identify lifecycle progression without requiring knowledge of cloud age. However, the authors also showed that this interpretation becomes ambiguous for multi-pulse clouds, in which renewed buoyant pulses transport moist air into the cloud and can temporarily increase r_t^*. As a result, different parts of the same cloud may simultaneously exhibit characteristics of growth and dissipation, complicating any unique definition of lifecycle stage.

Cloud lifecycle complexity extends beyond its visible boundaries, into its surroundings. Numerous studies document a moist halo surrounding shallow cumuli, a region just outside the cloud that is moister than the far environment and distinct from the downdraft shell (Radke and Hobbs, 1991; Perry and Hobbs, 1996; Lu et al., 2003; Laird, 2005; Schmeissner et al., 2015; Ackerman, 1958). Halo prevalence and spatial extent generally increase with cloud age (Laird, 2005; Gu et al., 2024); halos have also been found to enhance shortwave absorption in the surrounding atmosphere, especially near cloud top (Lu et al., 2002, 2003). However, the evolution of the halo through the cloud life cycle, especially during the dissipation, and its link to the underlying cloud microphysics remain only partly understood.

Satellite observations often provide instantaneous snapshots of cloud fields, which limits the ability to diagnose lifecycle-dependent behavior and related feedback (Quaas et al., 2020). Geostationary platforms can partially address this limitation by offering time-resolved observations over a fixed region, but typically at the cost of reduced spatial and spectral detail compared with polar-orbiting sensors. As a result, directly constraining the full evolution of individual shallow cumuli remains observationally challenging.

Accounting for the cloud life cycle has the potential to improve convection parameterizations (Neggers and Griewank, 2021; Cho, 1977). Most conventional convection schemes in large-scale coarse-resolution models represent shallow convection using a steady-state assumption, treating the properties of convective elements as quasi-stationary and not explicitly evolving. In addition, observations and simulations show that shallow cumuli often evolve through pulse-like events rather than a simpale life cycle of a continuously steady plumes (Heus et al., 2009; Grinnell et al., 1996; French et al., 1999; Scorer and Ludlam, 1953; Lim and Hoffmann, 2024; Katzwinkel et al., 2014; Zhao and Austin, 2005a, b). Representing this temporal evolution may be important for accuratly capturing cloud properties and related phenomena, such as the transition from shallow to deep convection (Kuang and Bretherton, 2006) and the emergence of convective organization into clusters (Neggers and Griewank, 2021). Recent work suggests that improved parameterizations should be based on physically consistent links between cloud

https://doi.org/10.5194/egusphere-2026-3677
Preprint. Discussion started: 10 July 2026

dynamics and microphysics rather than on steady plume assumptions alone (Khain et al., 2024). Therefore, improving convection parameterizations requires a better process-level understanding of how dynamical, microphysical, and thermodynamic factors control the growth and dissipation of shallow cumulus clouds.

The dissipation stage of shallow cumulus clouds is less well constrained than the growth and mature stages. Observational studies have provided partial insight into dissipating clouds. For example, Katzwinkel et al. (2014) described dissolving clouds as characterized by negative buoyancy and downdrafts. More detailed in situ measurements by Schmeissner et al. (2015) showed that dissipating clouds exhibit substantially reduced liquid water content compared to developing clouds, along with distinct microphysical characteristics, including a decrease in droplet number concentration while droplet sizes remain nearly unchanged. In contrast to the nearly unchanged droplet sizes reported bySchmeissner et al. (2015), Lim and Hoffmann (2024) used a Lagrangian LES model and found that for both polluted and clean clouds, the mean droplet radius tends to increase with cloud lifetime, while droplet number concentration decreases. Zhang et al. (2011) used LES bin microphysics model to examine the vertical evolution of droplet effective radius during cloud dissipation and showed that polluted and moderately polluted clouds tend to exhibit smaller ($\sim$10%) effective radius during the decaying stage, whereas clean clouds show larger effective radius and greater variability due to the additional influence of collision-coalescence and sedimentation processes. Both observational and numerical studies still have important gaps in understanding the dynamic, thermodynamic, and microphysical processes that govern the dissipation, how they vary with height, and evolve throughout time.

The present study focuses on the dissipation stage of isolated shallow cumulus clouds and on the evolution of their near-cloud environment. This study is a natural continuation of previous work on the dynamics, microphysics, and turbulence structure of shallow cumulus clouds, aimed at improving process-level understanding and ultimately the parameterization of shallow convection (Khain et al., 2024; Pinsky and Khain, 2023; Pinsky et al., 2021; Eytan et al., 2022; Arieli et al., 2024, 2026a, 2025a, b). Using high-resolution simulations of single clouds across a range of initial CCN concentrations, we examine how dissipation evolves in time, how it can be identified from bulk cloud properties and vertical structure, and how the decaying cloud modifies its surroundings.

2 Methods

We used the **S**ystem for **A**tmospheric **M**odeling (SAM) (Khairoutdinov and Randall, 2003) coupled with the Spectral Bin Microphysics (SBM) scheme (Khain et al., 2004) and an aerosol regeneration scheme (Arieli et al., 2025b, a) to simulate trade cumulus clouds following the Barbados Oceanographic and Meteorological Experiment (BOMEX) case setup (Siebesma et al., 2003; Friedman et al., 1970). The setup includes large-scale forcing and is initialized with vertical profiles of water vapor mixing ratio and potential temperature, with an inversion layer located between approximately 1500 and 2000 m. The surface fluxes were kept constant, and the background advection was set to zero to maintain the cloud near the center of the domain. Cloud initiation was triggered using a thermal perturbation of 0.1 K. In the SBM scheme, dry aerosol particles are represented using 39 size bins with radii up to 8 μm, and cloud droplets are represented using 33 size bins starting at 2 μm. Activation is explicitly treated according to Köhler theory: at each time step, the critical dry aerosol radius is diagnosed from

https://doi.org/10.5194/egusphere-2026-3677
Preprint. Discussion started: 10 July 2026

the local supersaturation, and dry aerosol bins with radii larger than this critical value are activated into droplets, after which the corresponding dry aerosol bins are emptied. Dry aerosols smaller than 0.33 μm are transferred to the smallest droplet bin (2 μm), whereas droplets formed on larger aerosols are assigned to droplet bins corresponding to a radius equal to six times the dry aerosol radius, followingKogan (1991).

We performed five single-cloud simulations with initial aerosol number concentrations of 25, 50, 250, 500, and 2000 cm^{-3}, uniformly distributed below cloud base, from the surface up to 600 m. The model domain was 5.12 km $\times$ 5.12 km in the horizontal with cyclic boundary conditions. The horizontal grid spacing was $dx = dy = 10$ m. The vertical grid spacing was $dz = 10$ m up to 3 km and 50 m in the uppermost kilometer, well above the cloud-top height. The model time step was $dt = 0.5$ s.

A cloud identification procedure was used to isolate the main cloud generated by the initial thermal perturbation, excluding secondary clouds from the analysis. Cloud objects were identified from a three-dimensional mask using a threshold of LWC $>$ 0.01 g kg^{-1}. At each time step, the analyzed cloud was defined as the connected object corresponding to the continuation of the initially triggered cloud; when splitting occurred, only the dominant fragment was retained.

3 Results

3.1 Dynamics of Dissipating Clouds

3.1.1 Bulk Evolution

We first examine the general evolution of the clouds during dissipation for the different CCN cases. The two cleanest cases (25 and 50 cm^{-3}) produced surface precipitation, whereas the more polluted cases (250, 500, and 2000 cm^{-3}) did not. Cross-sections of the cloud liquid water content (LWC) at selected times are shown in Fig. 1. During the developing stage, all clouds show increasing LWC with height, with the largest values near the cloud top. As the clouds evolve, clear differences emerge between the clean and polluted cases: in the clean simulations, dissipation is strongly influenced by precipitation, whereas in the polluted simulations, the clouds do not precipitate and decay mainly through evaporation and mixing. The figure also suggests narrowing of the cloudy region during dissipation, especially in the polluted cases; the responsible processes are examined in more detail below.

Figure 2 presents the clouds' evolution through time series of several bulk properties for all simulated cases. They are calculated for the cloudy voxels of the main cloud only, defined by LWC $>$ 0.01 g kg^{-1} and located above 600 m (cloud base). These bulk properties provide an integrated description of the cloud state and can therefore be useful for identifying the signature of the different stages along the cloud's lifecycle. The peaks in cloud-mean LWC (Fig. 2a) and cloud-top height (Fig. 2d), together with the first transition of the mean buoyancy from positive to negative (Fig. 2c), occur within a relatively narrow time window, between 32–35 min, across all simulations. By contrast, the maxima in cloud volume (Fig. 2e) and cloud area (Fig. 2f) occur later, after 35 min, and show larger differences among the cases. For cloud volume, cloud area, and cloud-total liquid mass (Fig. 2b), the precipitating cases peak a few minutes later than the non-precipitating cases, reflecting the onset

https://doi.org/10.5194/egusphere-2026-3677
Preprint. Discussion started: 10 July 2026

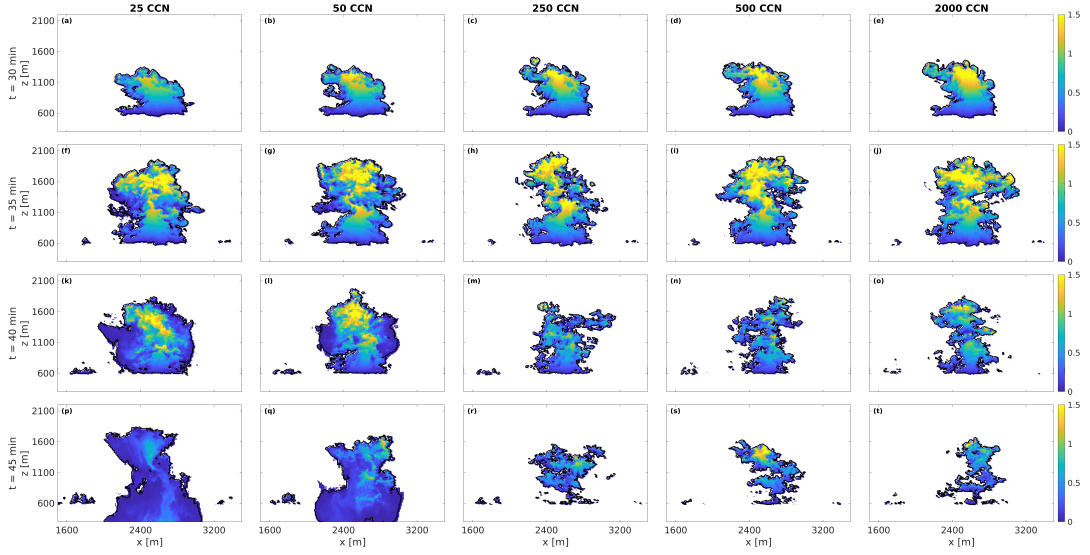

Figure 1. Vertical cross-sections of the liquid water content (LWC) field [$g\ kg^{-1}$]. Black contours indicate the cloud boundary defined by $LWC > 0.01\ g\ kg^{-1}$. Columns correspond to simulations initialized with different CCN concentrations (left to right): 25, 50, 250, 500, and 2000 cm^{-3}. Rows represent different time instants during the cloud evolution (30, 35, 40, and 45 min). Secondary small clouds are not analyzed.

of rain formation and the spread of falling hydrometeors along the cloud sides, which increase the apparent cloud extent and volume. Taken together, these differences show that individual variables can suggest different times for the transitions between lifecycle stages, highlighting the ambiguity in defining a single transition point.

Nevertheless, cloud-mean buoyancy together with cloud-top height provides a practical, though imperfect, basis for separating the cloud evolution into three stages. The growth stage is characterized by increasing positive buoyancy together with increasing cloud top height. The mature stage begins when the buoyancy reaches its maximum and extends until the subsequent transition to negative values. This coincides with the time when the cloud top first reaches the inversion layer ($\approx 1500\ m$), at approximately 30–31 min. During the following few minutes, the cloud continues to grow vertically, but its buoyancy begins to decrease. The dissipation stage begins around 33–35 min, when the cloud-mean buoyancy becomes negative, and the cloud's top stops rising. Within this definition, the dissipation stage lasts longer than the growth and mature stages combined. During this stage, the cloud no longer exhibits sustained vertical growth: cloud-top height decreases on average, although it continues to oscillate. At the same time, the mean buoyancy becomes negative overall, but also oscillates and can temporarily return to positive values. These oscillations are consistent with the cloud interacting with the very stable inversion layer, where oscillatory motions can be expected. Thus, the onset of negative mean buoyancy together with a decrease in cloud-top height and the subsequent oscillatory behavior of both variables provides a more robust indication of dissipation than buoyancy alone. This interpretation is consistent with the stage definitions of Katzwinkel et al. (2014), based on the 90th percentiles of in-cloud buoyancy and vertical velocity, in which actively growing clouds are positively buoyant with updrafts, decelerated clouds are

https://doi.org/10.5194/egusphere-2026-3677
Preprint. Discussion started: 10 July 2026

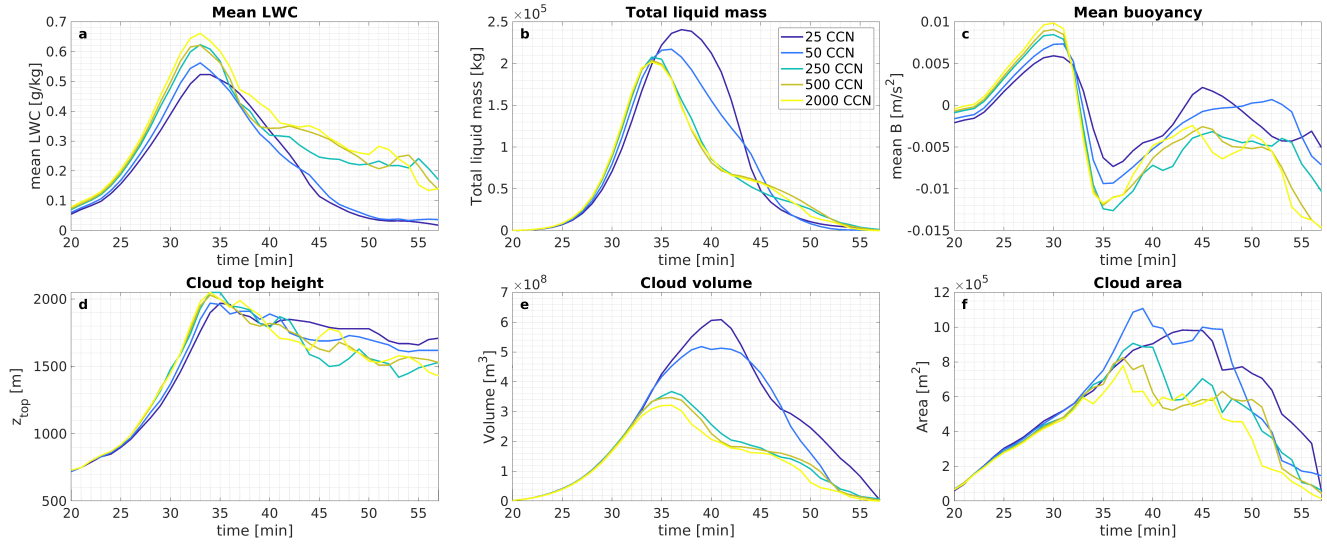

Figure 2. Time series of (a) cloud-mean liquid water content (LWC) $[g/kg]$, (b) cloud-total liquid mass $[kg]$ (c) cloud mean buoyancy $[m/s^2]$, (d) cloud-top height $[m]$, (d) cloud volume $[m^3]$, and (d) cloud area $[m^2]$. Curves correspond to simulations initialized with different CCN concentrations. For the precipitating cases, the cloud mask is defined only above 600 m (cloud base).

negatively buoyant but still exhibit updrafts, and dissipating clouds are negatively buoyant with downdrafts in their interior. Figure 2f shows the evolution of cloud area, which represents the cloud's top-down horizontal signature. In both the precipitating and non-precipitating cases, the maximum cloud area is reached during the early dissipation stage rather than during the mature stage. This behavior reflects the development of a horizontal spreading due to detrainment, which broadens the cloud after vertical growth has ceased. An important implication is that, in a satellite snapshot, the largest clouds are not necessarily the most actively growing ones; they may already be in the process of dissipation.

These results show that the boundaries between growth, maturity, and dissipation are not sharply defined, and that no single bulk variable provides a unique marker of the cloud lifecycle stage. The time series presented here demonstrates that bulk cloud properties must be tracked over time in order to identify the cloud lifecycle stage with confidence. Consequently, identifying the lifecycle stage from a single snapshot, whether from satellite imagery, radar observations, or an instantaneous model field, remains inherently challenging. In the following text and figures, we therefore focus on characteristics of the cloud and its immediate environment that can distinguish an early, actively growing cloud from a cloud in an advanced stage of dissipation.

3.1.2 Vertical Structure

Figure 3a–e shows a Hovmöller diagram of the horizontally averaged vertical velocity per height level as a function of time, and panels f–j show the corresponding horizontally averaged buoyancy.

All clouds reach the inversion base near $1500\ m$ at approximately 30 min and penetrate it, reaching top heights of about $2000\ m$. Upon reaching the inversion, buoyancy in the upper cloud becomes negative, yet the vertical velocity remains positive for

https://doi.org/10.5194/egusphere-2026-3677
Preprint. Discussion started: 10 July 2026

several minutes due to upward momentum, eventually turning negative aloft. This transition marks the initiation of cloud dissipation. In the precipitating cases, these upper-level downdrafts intensify and propagate downward as precipitation develops, since the falling rain enhances downward motion through drag and evaporative cooling. Alternating upward and downward motions near cloud top, reflected in repeated sign changes of the vertical velocity, are evident in all cases, suggesting that these oscillations are associated with the cloud interacting with the very stable inversion layer. In the non-precipitating cases, the lower part of the cloud remains positively buoyant and continues to exhibit pulse-like behavior, similar to the pulses described by Heus et al. (2009). While the upper part of the cloud is already negatively buoyant and dissipating, these lower-cloud pulses continue to transport moist, buoyant air upward, allowing positive buoyancy to persist into the late stages of the cloud lifetime (Fig. 3h-j). Once the supply of positively buoyant air from cloud base weakens, the lower-cloud updraft also weakens.

The bottom row of Fig. 3 shows the liquid-water mixing-ratio tendency due to condensation and evaporation (red indicates condensation; blue indicates evaporation). Evaporation dominates a thin layer near the clouds' top even during the growth phase, consistent with small-scale turbulence at the cloud edge that enhances mixing with dry environmental air (Arieli et al., 2024; Eytan et al., 2022; Wang and Geerts, 2010). During dissipation, the evaporative layer deepens progressively, but its downward expansion differs between the precipitating and non-precipitating cases. In the precipitating clouds, evaporation extends rapidly downward as precipitation-induced downdrafts develop. These downdrafts enhance downward transport and mixing, while the evaporation of falling hydrometeors promotes evaporative cooling and further strengthens the descending motion. As a result, evaporation affects a larger fraction of the cloud depth. In the non-precipitating clouds, the downward expansion of the evaporative layer is more gradual. Positive buoyancy pulses in the lower part of the clouds continue to support condensation for a longer part of the dissipation stage. This downward expansion is consistent with the weakening of positive buoyancy in the lower part of the clouds and the strengthening of negative buoyancy near the clouds' top (Fig.3h-j), which together reduces the upward transport of moist air from below. As a result, the evaporative cooling and downdrafts extend progressively to lower levels of the clouds.

3.1.3 Coherent and Turbulent Motions

The longer duration of the dissipation stage suggests that the processes governing cloud growth and decay are not symmetric. To examine this difference, we compare the relative contributions of convective-scale and turbulent motions. Figure 4a presents the time series of cloud-total turbulent kinetic energy (TKE) and cloud-total convective kinetic energy (CKE) (see Appendix A1 for the calculation method), while Fig. 4b shows the corresponding ratio of cloud-total TKE to CKE. Here, CKE represents the kinetic energy associated with convective-scale motions, whereas TKE represents the kinetic energy of turbulent motions with characteristic scales smaller than 100 m. In Fig. 4b, values below 1 indicate that the flow is dominated by coherent, large-scale convective motions, whereas values above 1 indicate turbulence-dominated flow.

In all cases, the growth stage is primarily convective, with TKE/CKE values well below 1, reflecting the dominance of organized, larger-scale circulations such as the toroidal vortex within the cloud (Eytan et al., 2024; Khain et al., 2024; Arieli et al., 2024, 2026a). As the clouds enter the dissipation stage, CKE decreases substantially, indicating a weakening of the coherent convective flow, while TKE continues to increase for an additional 2–4 min before reaching its maximum and then decreas-

https://doi.org/10.5194/egusphere-2026-3677
Preprint. Discussion started: 10 July 2026

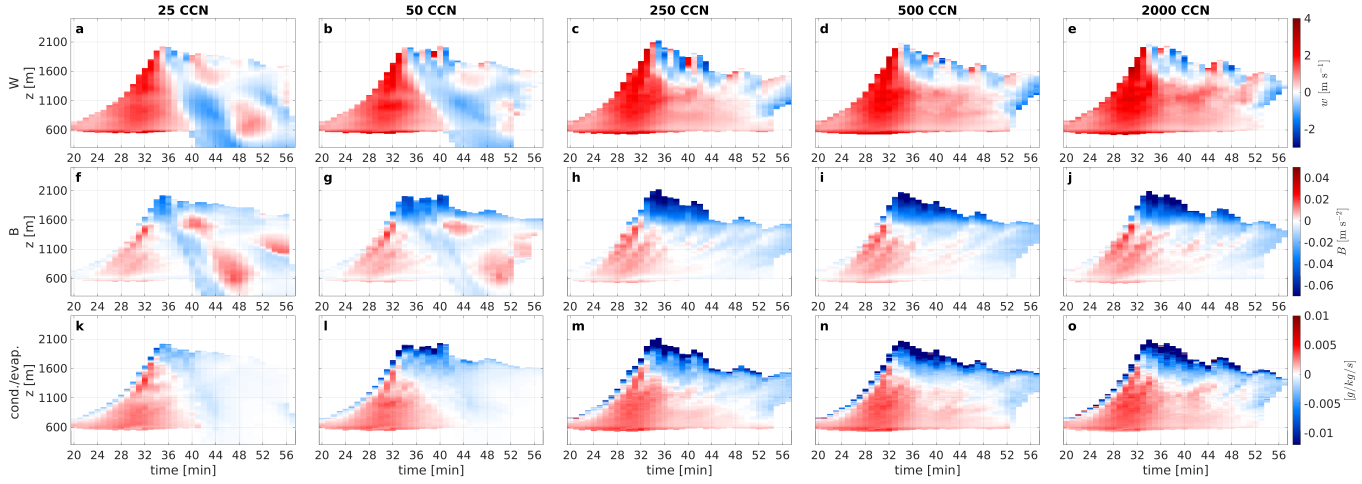

Figure 3. Hovmöller diagrams of horizontally averaged fields: top row - vertical velocity $[m/s]$, middle row - buoyancy $[m/s^2]$, and bottom row - liquid-water mixing-ratio tendency due to condensation/evaporation $[g/kg/s]$. Columns correspond to simulations initialized with different CCN concentrations (left to right): 25, 50, 250, 500, and 2000 cm^{-3}.

ing more gradually. This delayed TKE maximum suggests that small-scale turbulence persists after the coherent convective circulation has already weakened. This result is consistent with previous work showing that turbulence is strongest near cloud top in dissipating clouds (Pinsky and Khain, 2023). Consequently, the TKE/CKE ratio in the non-precipitating cases increases during dissipation, and turbulence becomes dominant during the advanced stages of dissipation, with TKE/CKE exceeding 1 after approximately 45 min. In the precipitating cases, the ratio initially rises toward a peak near the onset of precipitation, but subsequently decreases as precipitation-driven downdrafts strengthen the convective-scale kinetic energy.

Overall, these results suggest a dynamical transition during the cloud life cycle: large-scale coherent motions, such as the toroidal circulation within the cloud, dominate during growth, whereas during dissipation these organized structures weaken and smaller-scale turbulence becomes increasingly important. The increasing role of small-scale motions in the late stage promotes a more gradual erosion of the cloud through local mixing with the surrounding environment. Because this small-scale, localized mixing acts more slowly than the coherent convective transport that dominates during growth, it likely contributes to the longer duration of the dissipation stage compared to the growth stage.

3.2 Microphysics of Dissipating Clouds

3.2.1 Droplet Number and Size Distribution

Figure 5a–e shows a Hovmüller diagram of the evolution of the horizontally averaged droplet number concentration. In the precipitating cases (Fig. 5a,b), droplet concentrations are reduced near cloud top once the clouds reach the inversion layer. As dissipation begins, this region of reduced concentration gradually extends downward through the cloud layer. This behavior is consistent with enhanced collision–coalescence (Fig. 6f,g) and the initiation of precipitation, which efficiently reduces

https://doi.org/10.5194/egusphere-2026-3677
Preprint. Discussion started: 10 July 2026

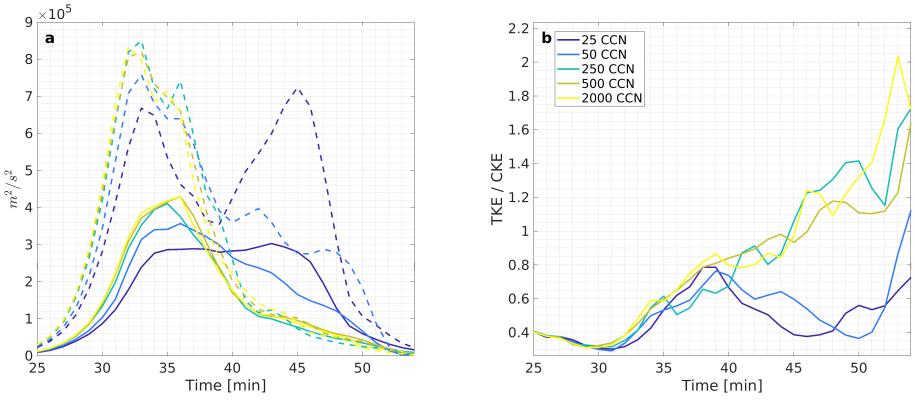

Figure 4. (a) Time series of cloud-total turbulent kinetic energy (TKE; solid lines) and cloud-total convective kinetic energy (CKE; dashed lines). (b) Time series of the ratio between cloud-total TKE and cloud-total CKE. Curves' colors correspond to simulations initialized with different CCN concentrations.

the number of droplets. In the more polluted, non-precipitating cases, the decrease is slighter and relatively larger droplet concentrations persist aloft, consistent with continued nucleation associated with regenerated aerosols (Fig. 6c,d,e).

Figure 5f–o shows two additional parameters, effective radius (Fig. 5f-i) and DSD width (Fig. 5k-o), for a full description of the evolution of the droplet size distribution (DSD). In the precipitating cases, the dissipation stage is characterized by a pronounced increase in both parameters, consistent with the emergence of a small population of large (rain) drops. By contrast, in the polluted non-precipitating cases, the drop effective radius (Fig. 5h-j) increases gradually with height, and this vertical structure remains broadly consistent over time. The DSD standard deviation (Fig. 5m-o) also tends to increase with height, but with a noisier and less smooth pattern, reflecting enhanced mixing near cloud top together with collision–coalescence and secondary nucleation (Fig. 6). Notably, the temporal variability of these microphysical properties is relatively weak compared to their vertical variability, suggesting that the dominant changes in the DSD are driven primarily by vertical processes. This behavior further suggests that turbulent mixing acts more slowly than the microphysical response: droplets exposed to entrained dry air evaporate rapidly, preferentially reducing droplet number concentration while maintaining a relatively similar mean droplet radius. This interpretation is consistent with (Lim and Hoffmann, 2024), who showed that inhomogeneous mixing becomes increasingly important over the cloud life cycle. This is also consistent with the ergodicity framework of Lensky and Rosenfeld (2006), who showed from satellite observations of convective clouds that droplet effective radius depends primarily on height and thermodynamic conditions, while exhibiting relatively weak temporal variability over the cloud lifetime. Similar behavior was reported in the in situ observations of Schmeissner et al. (2015), who found that dissipating clouds exhibit reduced liquid water content and droplet number concentration, whereas droplet sizes remain nearly unchanged relative to developing clouds. Overall, for the non-precipitating clouds, vertical profiles of effective radius and DSD standard deviation are poor indicators of cloud age because their structures evolve only weakly over their lifetimes.

https://doi.org/10.5194/egusphere-2026-3677
Preprint. Discussion started: 10 July 2026

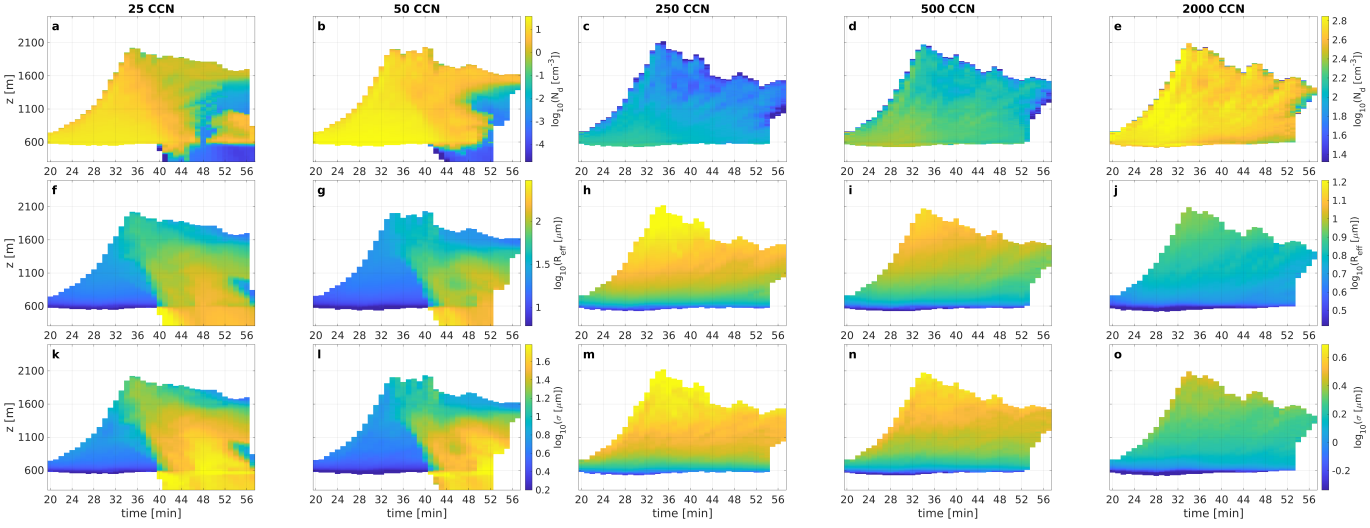

Figure 5. Hovmöller diagrams of horizontally averaged cloud microphysical properties plotted on a logarithmic color scale. The top row shows droplet number concentration [cm^{-3}], the middle row shows effective radius [μm], and the bottom row shows standard deviation of the drop size distribution (DSD) [μm]. Columns correspond to simulations initialized with different CCN concentrations (left to right): 25, 50, 250, 500, and 2000 cm^{-3}. Within each row, the two leftmost panels (precipitating cases) and the three rightmost panels (non-precipitating cases) use separate color scales to better visualize their respective value ranges. The corresponding Hovmöller diagrams plotted using linear color scales are shown in Supplementary Figure S1.

3.2.2 Nucleation and Collision–Coalescence Processes

Examining the tendencies associated with nucleation and collision–coalescence (Fig. 6) clarifies how microphysical processes evolve as clouds enter the dissipation. In the non-precipitating clouds, nucleation increases in the upper part of the cloud at the onset of dissipation. This enhancement is linked to aerosol regeneration: droplets transported to higher levels evaporate, releasing aerosol particles that can subsequently reactivate under supersaturated conditions (Arieli et al., 2025a). As shown in Fig. 3a–e, oscillations in vertical velocity near cloud top generate conditions of supersaturation (Hovmöller diagrams of the saturation ratio are shown in Fig. S2), promoting activation of regenerated aerosol. Although the mean saturation ratio in the upper part of the cloud is negative during this stage (Fig.S2a-e), Fig. S2f-j shows that the 90th percentile represents supersaturated conditions, indicating intermittent regions favorable for renewed nucleation. These nucleation events weaken with time along the dissipation stage, together with the weakening of the cloud's updraft.

The collision–coalescence tendency evolves differently. It peaks near the time of maximal cloud growth, when the liquid water content and updraft strength are the largest (see Fig. 1), and then decreases as the cloud dissipates. In the precipitating clouds, the region of enhanced collision–coalescence extends downward following the onset of precipitation, reflecting the formation and descent of rain.

https://doi.org/10.5194/egusphere-2026-3677
Preprint. Discussion started: 10 July 2026

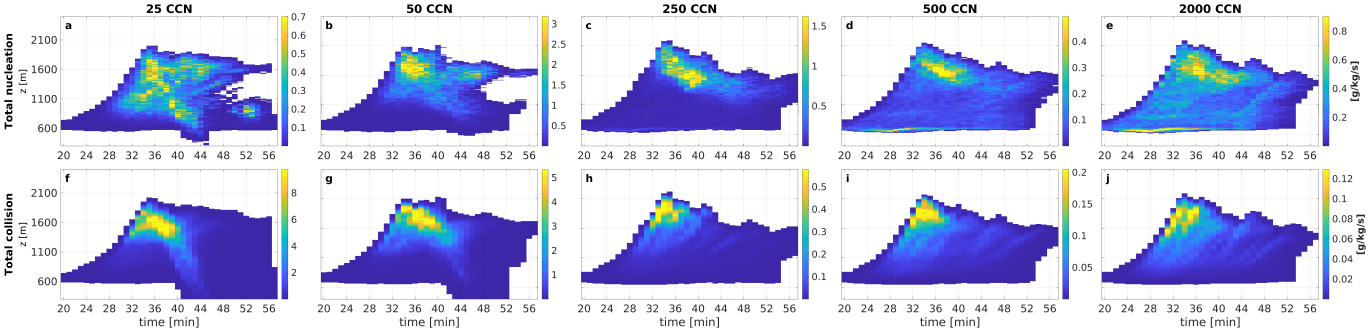

Figure 6. Hovmöller diagrams of horizontally summed fields: top row - liquid-water mixing-ratio tendency from nucleation $[g/kg/s]$, and bottom row - liquid-water mixing-ratio tendency $[g/kg/s]$ from collision–coalescence. Columns correspond to simulations initialized with different CCN concentrations (left to right): 25, 50, 250, 500, and 2000 cm^{-3}. Note that each panel uses a different color scale.

3.2.3 Radial Structure

Figure 7 shows the liquid water content (LWC) and vertical velocity as functions of height and distance from the cloud edge (DFCE) at different times during the cloud lifetime, providing a view of the radial structure of the clouds. This figure corresponds to the simulation initialized with 500 cm^{-3} CCN (non-precipitating cloud). Here, DFCE is defined only within the cloud interior, so negative values correspond to increasing distance from the cloud edge toward the cloud center. Figure 8 presents horizontal cross-sections of the LWC, vertical velocity, and saturation fields at $1500\ m$ height for different times, while Fig.S3 shows the corresponding fields at $900\ m$. During the mature stage (Fig. 7a,e and Fig. 8a,e), both the LWC and the vertical velocity decrease toward the cloud edge, with the largest values located in the inner and upper parts of the cloud. As dissipation begins, the upper-level downdrafts that were identified in Fig. 3i appear clearly in Fig. 7f–h, primarily near the upper cloud edge. At the same time, the inner and lower parts of the cloud continue to exhibit positive vertical velocity.

As can be seen in Fig. 8, regions of reduced LWC are closely associated with downdrafts, and they also coincide with lower saturation values, indicating enhanced evaporation in descending air. This relationship highlights the important role of downdrafts in cloud dissipation. In addition, the evolution of LWC (Fig. 7a–d) shows a progressive reduction over time: LWC decreases first near the cloud edges and only later in the cloud interior. This behavior most likely results from the combined effects of weakening of the core updraft, which reduces the supersaturation, and enhanced lateral mixing that progressively penetrates into the inner part of the cloud.

Figure 9 shows the same analysis as Fig. 7, but for the precipitating cloud (initialized with 50 cm^{-3} CCN). At the onset of dissipation (panels b,f), downdrafts are primarily located near the cloud top. As shown in Fig.8f, the horizontal cross-sections indicate that the downdrafts occupy most of the cloud's horizontal extent. At the same time, an updraft core persists in the inner part of the cloud, where higher LWC values and supersaturation are also found. Later along the dissipation, the falling of precipitation leads to stronger and more widespread downdrafts, while localized updraft regions with higher LWC (Fig. 9c,g, Fig. 8 and Fig.S4) can still be observed. Overall, these results show that during the mature stage, the cloud's radial

https://doi.org/10.5194/egusphere-2026-3677
Preprint. Discussion started: 10 July 2026

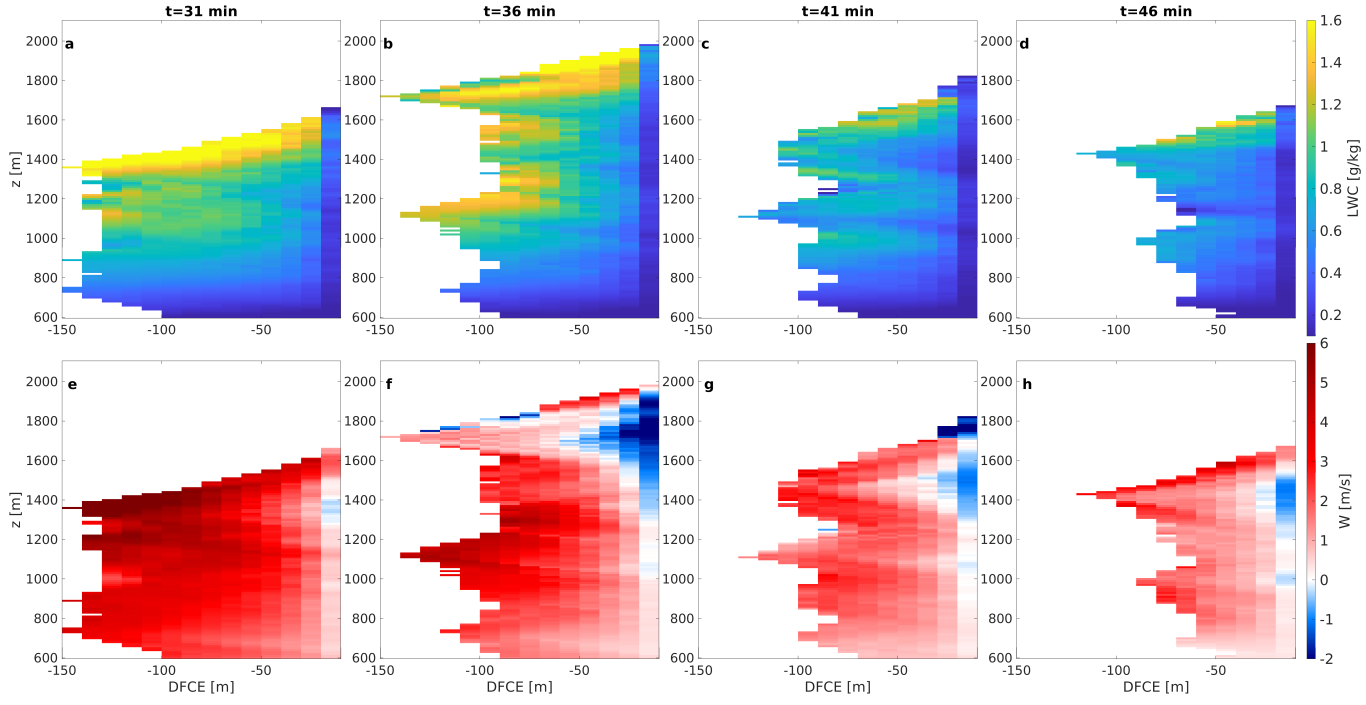

Figure 7. Cloud variables in z–DFCE coordinates. The upper row shows liquid water content (LWC) $[g/kg]$, and the lower one shows vertical velocity $[m/s]$. The x-axis represents the distance from the cloud edge (DFCE), with negative values indicating points inside the cloud. The y-axis denotes height. Each column corresponds to a different time during the cloud evolution (31, 36, 41, and 46 min). Results are shown for the simulation initialized with 500 cm^{-3} CCN. The fields are horizontally averaged at each height by binning data according to DFCE, using bin widths of 10 m.

structure is characterized by a clear core with large LWC and strong updrafts. Later, during dissipation, this structure becomes more fragmented: low-LWC and sub-saturated regions, together with downdrafts, first appear in the upper levels and near the cloud edges, then progressively extend inward. At the same time, the cloud retains an updraft core for part of the dissipation stage, particularly in the inner and lower regions. This pattern highlights the important roles of downdrafts, lateral mixing, and detrainment in controlling cloud decay, and demonstrates that dissipation is non-uniform in both the radial and vertical directions, rather than a uniform weakening of the cloud as a whole.

3.3 Near-Cloud Environment During Dissipation

To characterize dissipation more comprehensively, we next examine the near-cloud environment. Vorticity and humidity anomalies develop outside the cloud. Figure 11 shows the enstrophy, computed from the vorticity $\boldsymbol{\omega} = \nabla \times \mathbf{V}$, where $\mathbf{V} = (u, v, w)$. In three dimensions,

$$\nabla \times \mathbf{V} = \left(\frac{\partial w}{\partial y} - \frac{\partial v}{\partial z}, \frac{\partial u}{\partial z} - \frac{\partial w}{\partial x}, \frac{\partial v}{\partial x} - \frac{\partial u}{\partial y} \right), \tag{1}$$

https://doi.org/10.5194/egusphere-2026-3677
Preprint. Discussion started: 10 July 2026

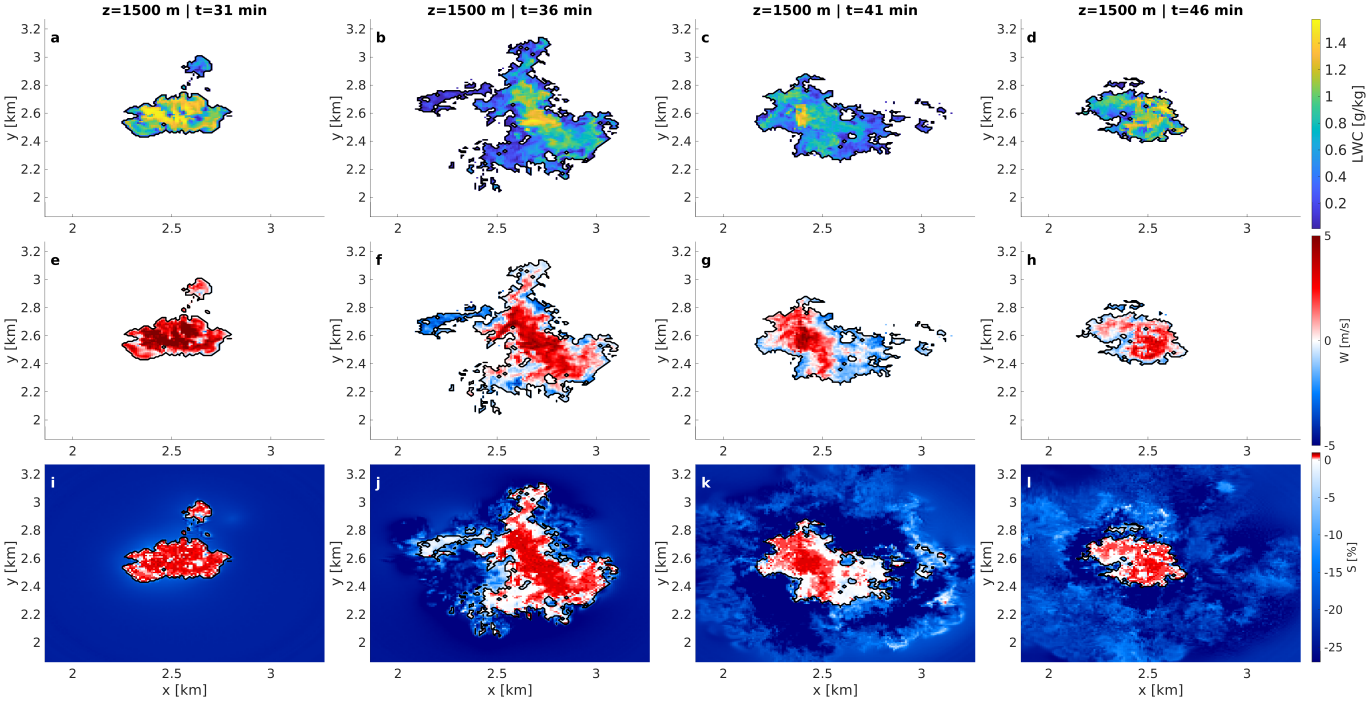

Figure 8. Horizontal cross-sections at a height of 1500 m. The upper panels show liquid water content (LWC) $[g/kg]$, the middle panels show vertical velocity $[m/s]$, and the lower panels show saturation $[\%]$. Rows correspond to different times during the cloud evolution (31, 36, 41, and 46 min). Results for the non-precipitating cloud initialized with 500 cm^{-3} CCN.

And the enstrophy is defined as

$$\mathcal{E} = \frac{1}{2}|\boldsymbol{\omega}|^2. \tag{2}$$

Figure 11a-e presents Hovmöller diagrams of $\mathcal{E}$ as a function of distance from the cloud edge, with DFCE defined here only outside the cloud, so that larger values correspond to locations farther into the surrounding environment. In all simulations, enstrophy intensifies outside the cloud as dissipation proceeds, indicating that the decaying cloud creates a persistent vorticity signature in its environment. The strongest signal occurs near the cloud edge, consistent with the strong velocity gradients at the cloud–environment interface. During dissipation, this enstrophy signal extends outward from the cloud edge, consistent with advection by detrainment flow into the surrounding air and with the reduction in cloud size. Panels f–j show the enstrophy anomaly relative to the mean enstrophy field averaged over all cases. This representation highlights the relative magnitude of enstrophy in each case compared with the mean behavior across the different CCN concentrations. These results indicate that the more polluted clouds leave a stronger enstrophy signal in their surroundings during the dissipation stage. Consistent with the existence of turbulence outside the visible cloud, Ackerman (1958) documented, from aircraft measurements, that enhanced turbulence was not confined to the visual cloud but extended into the surrounding clear air, often forming an asymmetric region of enhanced clear-air turbulence adjacent to the downshear of tropical cumuli.

https://doi.org/10.5194/egusphere-2026-3677
Preprint. Discussion started: 10 July 2026

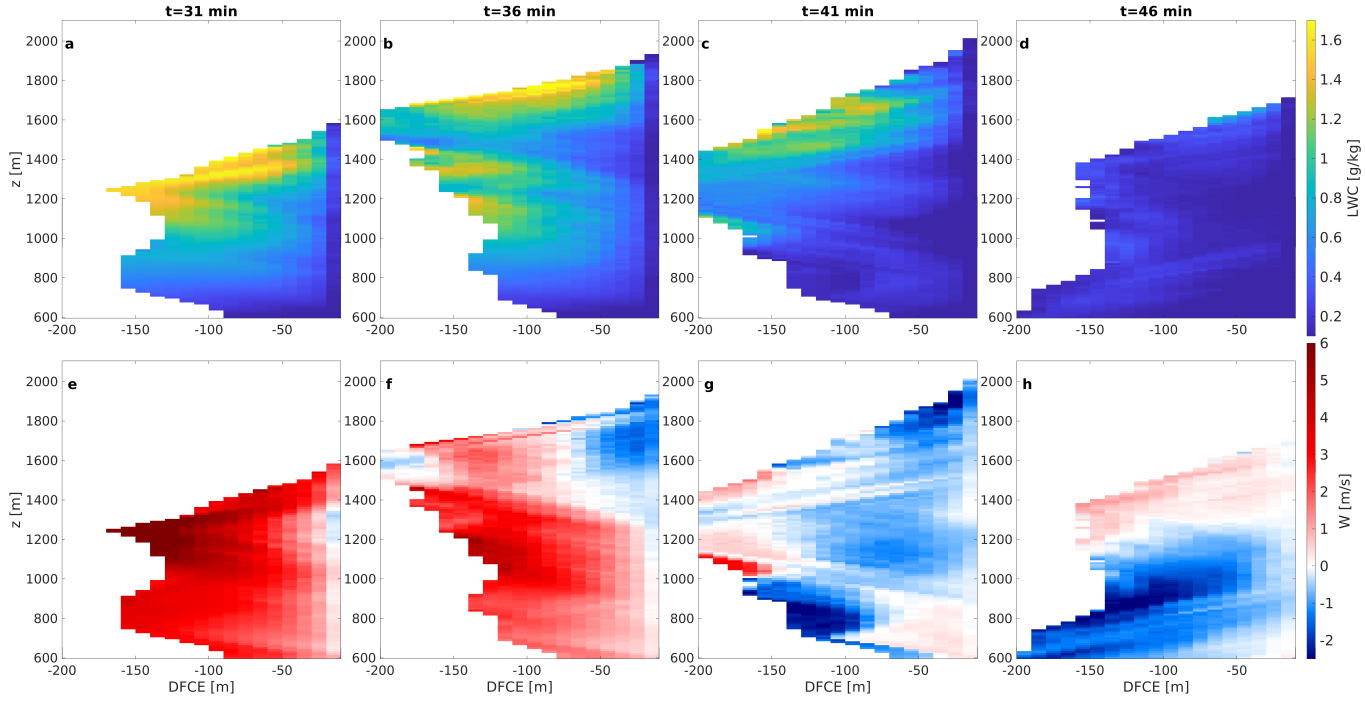

Figure 9. Cloud variables in z–DFCE coordinates. The upper row shows liquid water content (LWC) $[g/kg]$, and the lower one shows vertical velocity $[m/s]$. The x-axis represents the distance from the cloud edge (DFCE), with negative values indicating points inside the cloud. The y-axis denotes height. Each column corresponds to a different time during the cloud evolution (31, 36, 41, and 46 min). Results are shown for the simulation initialized with 500 cm^{-3} CCN. The fields are horizontally averaged at each height by binning data according to DFCE, using bin widths of 10 m.

Figure 12 is similar to Fig. 11, but the color shading shows the relative humidity (RH) anomaly relative to the initial profile. As the clouds dissipate, they leave a clear environmental imprint: a region of enhanced RH anomaly develops around the cloud edge, and the area (extent) of this large RH anomaly increases during the dissipation stage. It is important to note, however, that this increase is not monotonic; both the intensity and the extent of the humid halo exhibit oscillations over time. In addition, a weaker positive RH anomaly is also present during the early growth stage, although it is less pronounced than the halo observed during dissipation. Figure 13 shows vertical cross-sections of the RH anomaly from the simulation initialized with 500 cm^{-3} CCN, while Fig. S5 presents the corresponding cross-sections for the clean case initialized with 50 cm^{-3} CCN. The humid halo is also apparent in the horizontal saturation cross-sections shown in Fig.8 and Fig.10, particularly during the advanced dissipation stage. The humid halo surrounding the cloud is evident in these snapshots and becomes progressively stronger and more spatially extended as the cloud enters the dissipation stage. However, the halo does not exhibit a uniform or well-defined structure: regions of negative RH anomaly are also present in the near-cloud environment, particularly during earlier dissipation stages (Fig.13c). Although during advanced dissipation (Fig. 13e,f), the positive RH anomaly becomes clearly dominant around

https://doi.org/10.5194/egusphere-2026-3677
Preprint. Discussion started: 10 July 2026

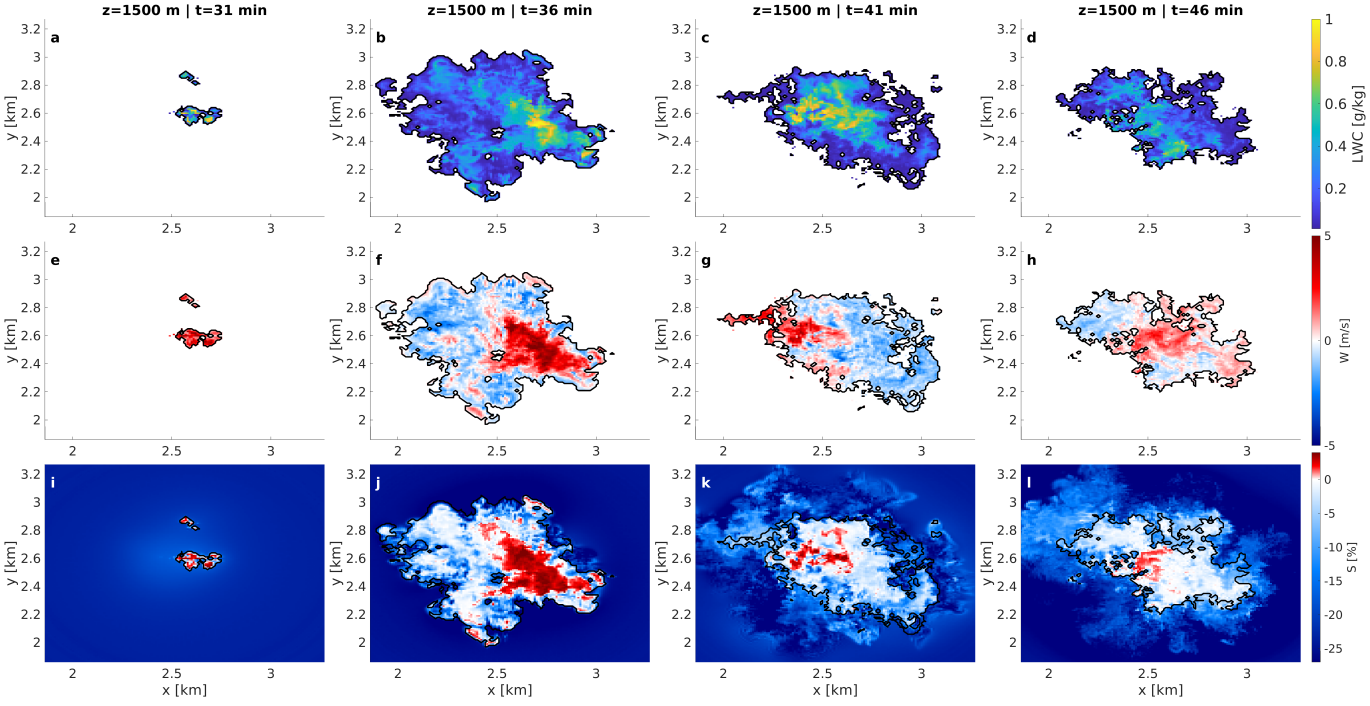

Figure 10. Horizontal cross-sections at a height of 1500 m. The upper panels show liquid water content (LWC) $[g/kg]$, the middle panels show vertical velocity $[m/s]$, and the lower panels show saturation $[\%]$. Rows correspond to different times during the cloud evolution (31, 36, 41, and 46 min). Results for the precipitating cloud initialized with 50 cm^{-3} CCN.

the cloud. This humidified halo has been reported previously in both observations (Perry and Hobbs, 1996; Laird, 2005) and simulations (Lu et al., 2002; Gu et al., 2024). Prior work found that the halo widens at later stages of the cloud lifecycle and can significantly influence radiative effects. Our results extend this picture by showing that halo evolution is neither smooth nor monotonic, but instead oscillates in both intensity and spatial extent over the cloud lifetime. In addition, our analysis shows that a weak moist halo is already present during the early growth stage, becomes a region of negative RH anomaly until the dissipation stage, and then strengthens markedly during advanced dissipation. Its spatial extent increases through a combination of detrainment from the cloud and the evaporation of small detached cloud fragments, leaving humid air in the surrounding environment. We further show that this humidity halo occurs in both precipitating and non-precipitating clouds.

4 Conclusions

In this study, we investigated the dissipation of isolated shallow cumulus clouds across a range of initial CCN concentrations using high-resolution simulations coupled with spectral bin microphysics and an aerosol regeneration scheme. The use of spectral bin microphysics together with an aerosol regeneration scheme is particularly important in this context because it allows for a more realistic representation of aerosol evolution during the late stages of cloud evolution and therefore provides a

https://doi.org/10.5194/egusphere-2026-3677
Preprint. Discussion started: 10 July 2026

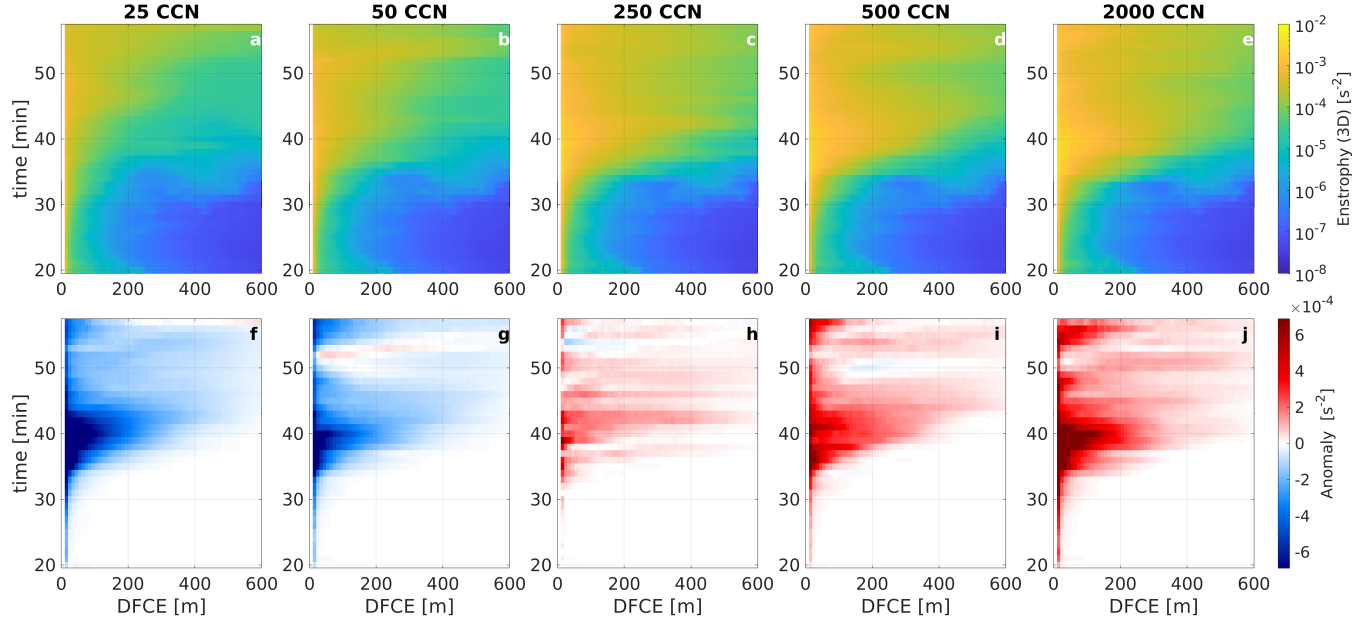

Figure 11. Hovmöller diagrams of distance from the cloud edge (DFCE; x-axis) as a function of cloud lifetime (y-axis). The upper row shows enstrophy (vorticity magnitude) averaged over the 600-2500 m layer, while the lower row shows enstrophy anomaly obtained by subtracting the mean enstrophy field averaged over all cases. DFCE is defined as positive outside the cloud, with larger values indicating greater distance from the cloud boundary. Columns correspond to simulations initialized with different CCN concentrations (left to right): 25, 50, 250, 500, and 2000 cm^{-3}. Note that the color scale is logarithmic.

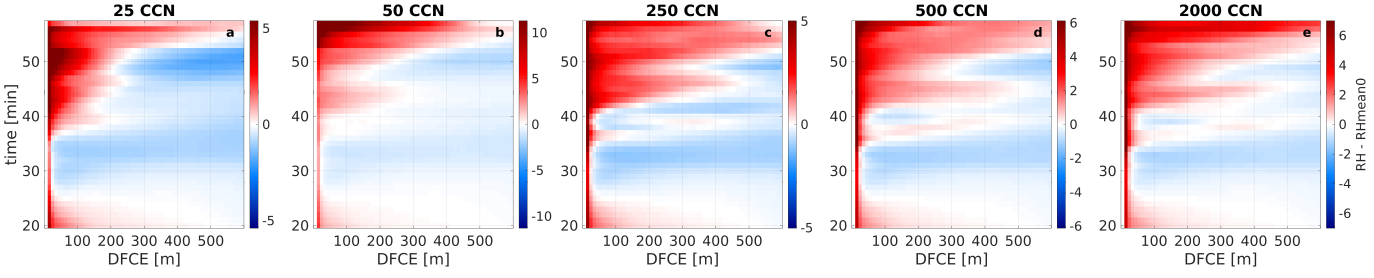

Figure 12. Hovmöller diagrams of the relative-humidity anomaly as a function of distance from the cloud edge (DFCE; x-axis). Color shading shows the relative-humidity anomaly, in percentage, with respect to the initial vertical RH profile, averaged over the 600–2500 m layer. Voxels associated with surrounding clouds larger than 2 voxels were excluded. Columns correspond to simulations initialized with different CCN concentrations (left to right): 25, 50, 250, 500, and 2000 cm^{-3}. Note that each panel uses a different color scale.

more physically consistent framework for investigating cloud dissipation and the formation of the near-cloud humid halo. This approach provides a process-based characterization of shallow cumulus dissipation and identifies signatures that distinguish dissipating clouds from growing clouds. Our results show that the dissipation stage is not marked by a sharp transition, but is

https://doi.org/10.5194/egusphere-2026-3677
Preprint. Discussion started: 10 July 2026

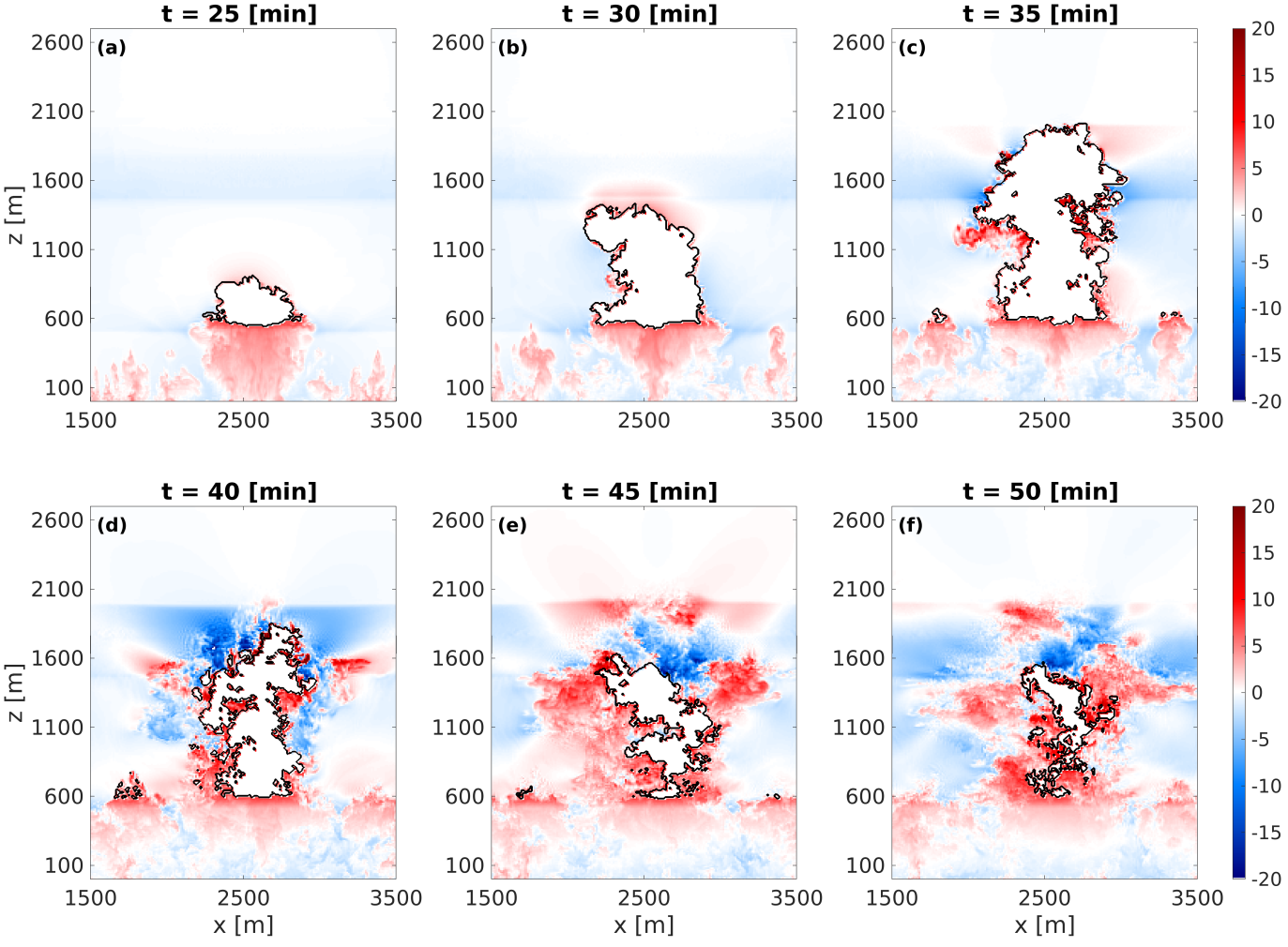

Figure 13. Vertical cross-sections from the 500 cm^{-3} CCN simulation. Color shading represents the relative humidity anomaly relative to the initial RH profile, while black contours mark the cloud boundary ($LWC > 0.01\ g\ kg^{-1}$). Panels show different times during the cloud evolution.

instead an extended, dynamically complex phase of cloud evolution. A classification based on cloud-mean buoyancy together with cloud-top height provides a practical framework for identifying the dissipation stage, although this framework is imperfect because moist air can continue to be supplied from cloud base, maintaining upward motion in the lower part of the cloud even after the upper part has begun to decay. Within this framework, the dissipation stage lasts longer than the growth and mature stages combined. During dissipation, cloud-top height oscillates while decreasing on average, and cloud-mean buoyancy is negative overall but can temporarily return to positive values. These oscillations are associated with the cloud interacting with the stable inversion layer. In addition, the horizontal cloud area reaches its maximum during early dissipation rather than during

https://doi.org/10.5194/egusphere-2026-3677
Preprint. Discussion started: 10 July 2026

the mature stage, implying that the largest clouds in instantaneous observations are not necessarily the most actively growing ones and that cloud fields can be biased toward dissipating clouds.

The dynamics of dissipation differ fundamentally from those of the growth stage. All simulated clouds penetrate the inversion layer at this stage, after which buoyancy near cloud top becomes negative while upward motion persists briefly because of inertia. A few minutes after the cloud top reaches the inversion, downdrafts begin to develop near cloud top, marking the onset of dissipation. At the same time, the lower part of the cloud can still be positively buoyant because moist air continues to be supplied from cloud base, maintaining upward transport and sustaining the cloud interior. The subsequent decay is accompanied by a progressive deepening of evaporative tendencies from cloud top downward, until evaporation dominates most of the cloud depth. This behavior reflects the non-uniform nature of cloud dissipation in both the radial and vertical directions: decay begins near the cloud top and edges and gradually propagates toward the cloud interior. As the updrafts and upward supply of moisture from cloud base weaken, erosion also proceeds from below, while the cloud continues to mix with the surrounding environment. During the growth stage, the flow is primarily coherent, with large-scale circulations, such as toroidal vortices. As dissipation progresses, these coherent structures weaken and the relative contribution of small-scale turbulence increases. The increasing role of small-scale turbulence during the late stages promotes a more gradual erosion of the cloud through mixing with the environment. Together with the continued upward supply of moist air from cloud base during the early stages of dissipation, this helps explain why the dissipation stage lasts substantially longer than the growth stage.

The microphysical evolution during dissipation depends strongly on aerosol loading and precipitation formation. In the precipitating cases, droplet number concentration decreases markedly near cloud top once the clouds reach the inversion, due to collision-coalescence, and this reduction progressively propagates downward through the cloud during dissipation. At the same time, effective radius and DSD width increase strongly, consistent with the formation of a relatively small number of large raindrops. In the more polluted, non-precipitating cases, these signatures are weaker: although droplet concentrations gradually decrease over time, they remain relatively high aloft throughout most of the cloud lifetime, while effective radius and DSD width profiles change only modestly with time, making them poor indicators of the cloud lifecycle stage.

Dissipation leaves a clear imprint on the surrounding environment, both in precipitating and non-precipitating clouds. Enstrophy increases outside the cloud as decay proceeds, indicating that dissipating clouds generate a persistent vorticity signature in the near-cloud region. The strongest enstrophy signal occurs near the cloud edge and extends outward during dissipation, consistent with vorticity generation by strong velocity gradients at the cloud–environment interface, followed by advection through detrainment. At the same time, a humid halo develops around the cloud edge and becomes stronger and larger during dissipation, although its evolution is not monotonic and exhibits oscillations in both intensity and extent. A weaker humidity halo is already present during initial growth, but the dissipation stage halo is substantially more pronounced. Its expansion is linked to both detrainment from the cloud and evaporation of small detached cloud fragments, leaving humid air in the surrounding environment. These signatures are consistently observed across all simulations, regardless of precipitation regime, indicating that they are a robust feature of shallow cumulus dissipation. These results show that cloud dissipation is a coupled evolution of cloud dynamics, microphysics, turbulence, and the near-cloud environment.

https://doi.org/10.5194/egusphere-2026-3677
Preprint. Discussion started: 10 July 2026

This study focuses on the BOMEX case study, which represents an idealized shallow trade cumulus environment. BOMEX is a well-studied and widely validated benchmark for shallow convection. We therefore expect many of the processes identified here to be representative of shallow trade cumulus clouds. Moreover, several features of the simulated dissipation stage are consistent with previous in situ observations and numerical studies, providing additional support for the robustness of our results. Nevertheless, the extent to which these findings can be generalized beyond the present conditions remains uncertain. Environmental conditions such as stronger wind shear, deeper or shallower convection, or different atmospheric stability may alter the structure and evolution of cloud dissipation.

Overall, our findings suggest that the dissipation of shallow cumulus clouds is a distinct and extended stage of cloud evolution characterized by weakening coherent circulation, an increased relative contribution of small-scale turbulence, progressive evaporation, and the development of turbulent and humid halos around the cloud. This decay is spatially non-uniform, progressing from the cloud top and edges toward the cloud interior. Because these signatures persist outside the visible cloud and because dissipation occupies a large fraction of the cloud lifetime, they may be especially relevant for interpreting snapshot observations and for improving representations of shallow convection in larger-scale models.

Code availability. The SAM codes are available on the website of Prof. Marat Khairoutdinov Khairoutdinov. The code and the data to reproduce the figures of the manuscript are publicly available at a repository Arieli et al. (2026b).

Appendix A: Appendix A

A1 Separation of Turbulent and Convective Kinetic Energy

To partition the flow into turbulent and convective components, motions with characteristic spatial scales smaller than 100 m were defined as turbulent, whereas larger-scale motions were classified as convective (Pinsky et al., 2021; Pinsky and Khain, 2023). These studies identified a transition between convective and turbulent motions at a separating wavenumber of approximately 1.15×10^{-2} m^{-1}, corresponding to a spatial scale of about 87 m, which represents the upper bound of the energy-containing turbulent eddies.

At each height, the coherent (convective) velocity field was computed by horizontally averaging the velocity over 100 m $\times$ 100 m squares, denoted here as $\overline{u}_{100}$, $\overline{v}_{100}$, and $\overline{w}_{100}$. The turbulent velocity components were then defined as deviations from this local mean:

$$u' = u - \overline{u}_{100}, \quad v' = v - \overline{v}_{100}, \quad w' = w - \overline{w}_{100}. \tag{A1}$$

The turbulent kinetic energy (TKE) was calculated as

$$TKE = \frac{1}{2}\left(u'^2 + v'^2 + w'^2\right). \tag{A2}$$

https://doi.org/10.5194/egusphere-2026-3677
Preprint. Discussion started: 10 July 2026

The convective (coherent) kinetic energy (CKE) was defined directly from the mean velocities as

$$CKE = \frac{1}{2}\left(\overline{u}_{100}^2 + \overline{v}_{100}^2 + \overline{w}_{100}^2\right). \quad \text{(A3)}$$

Author contributions. Y.A. led the study and conducted the simulations and analysis. Y.A., A.K, O.A., E.G., and I.K. conceptualized the research and discussed the results. Y.A. wrote the original manuscript draft. All Authors reviewed and edited the manuscript.

Competing interests. The contact author has declared that none of the authors has any competing interests.

Acknowledgements. This project has received funding from the European Research Council (ERC) under the European Union's Horizon 2020 research and innovation programme (CloudCT, grant agreement No 810370), and by The Israel Science Foundation (grants 2635/20; 1449/22).

https://doi.org/10.5194/egusphere-2026-3677
Preprint. Discussion started: 10 July 2026

References

Ackerman, B.: TURBULENCE AROUND TROPICAL CUMULI, https://journals.ametsoc.org/view/journals/atsc/15/1/1520-0469_1958_015_0069_tatc_2_0_co_2.xml, 1958.

Arieli, Y., Eytan, E., Altaratz, O., Khain, A., and Koren, I.: Distinct mixing regimes in shallow cumulus clouds, Geophysical Research Letters, 51, e2023GL105 746, 2024.

Arieli, Y., Khain, A., Gavze, E., Altaratz, O., Eytan, E., and Koren, I.: The Impact of Regenerated Aerosols on the Microphysics of Cumulus Clouds, Journal of the Atmospheric Sciences, 82, 2491–2503, 2025a.

Arieli, Y., Khain, A., Gavze, E., Altaratz, O., Eytan, E., and Koren, I.: The Impact of Cumulus Clouds and CCN Regeneration on Aerosol Vertical Distribution and Size, Journal of the Atmospheric Sciences, 82, 107–118, 2025b.

Arieli, Y., Altaratz, O., Khain, A., and Koren, I.: Investigating the Periphery Region in Warm Cumulus Clouds, Geophysical Research Letters, 53, e2025GL120 944, https://doi.org/10.1029/2025GL120944, _eprint: https://agupubs.onlinelibrary.wiley.com/doi/pdf/10.1029/2025GL120944, 2026a.

Arieli, Y., Khain, A., Altaratz, O., Gavze, E., and Koren, I.: Dataset for: The Dissipation of Shallow Cumulus Clouds: Dynamics, Microphysics, and Environmental Signatures, https://doi.org/10.34933/820bf2a9-4ff2-48a8-b7ba-d3987ab91476, 2026b.

Cho, H.-R.: Contributions of Cumulus Cloud Life-Cycle Effects to the Large-Scale Heat and Moisture Budget Equations, https://journals.ametsoc.org/view/journals/atsc/34/1/1520-0469_1977_034_0087_cocclc_2_0_co_2.xml, 1977.

Eytan, E., Khain, A., Pinsky, M., Altaratz, O., Shpund, J., and Koren, I.: Shallow Cumulus Properties as Captured by Adiabatic Fraction in High-Resolution LES Simulations, Journal of the Atmospheric Sciences, 79, 409 – 428, https://doi.org/10.1175/JAS-D-21-0201.1, place: Boston MA, USA, 2022.

Eytan, E., Arieli, Y., Khain, A., Altaratz, O., Pinsky, M., Gavze, E., and Koren, I.: The Role of the Toroidal Vortex in Cumulus Clouds' Entrainment and Mixing, Journal of Geophysical Research: Atmospheres, 129, e2023JD039 493, https://doi.org/10.1029/2023JD039493, 2024.

French, J. R., Vali, G., and Kelly, R. D.: Evolution of small cumulus clouds in Florida: observations of pulsating growth, Atmospheric Research, 52, 143–165, https://doi.org/10.1016/S0169-8095(99)00024-1, 1999.

Friedman, H. A., Conrad, G., and McFadden, J. D.: ESSA research flight facility aircraft participation in the Barbados Oceanographic and Meteorological Experiment, Bulletin of the American Meteorological Society, 51, 822–835, 1970.

Grinnell, S. A., Bretherton, C. S., Fraser, A. M., and Stevens, D. E.: Vertical Mass Flux Calculations in Hawaiian Trade Cumulus Clouds from Dual-Doppler Radar, https://journals.ametsoc.org/view/journals/atsc/53/13/1520-0469_1996_053_1870_vmfcih_2_0_co_2.xml, 1996.

Gu, J.-F., Plant, R. S., Holloway, C. E., and Clark, P. A.: The moist halo region around shallow cumulus clouds in large eddy simulations, Quarterly Journal of the Royal Meteorological Society, 150, 1501–1517, https://doi.org/10.1002/qj.4656, _eprint: https://rmets.onlinelibrary.wiley.com/doi/pdf/10.1002/qj.4656, 2024.

Heus, T., Jonker, H. J. J., Van den Akker, H. E. A., Griffith, E. J., Koutek, M., and Post, F. H.: A statistical approach to the life cycle analysis of cumulus clouds selected in a virtual reality environment, Journal of Geophysical Research: Atmospheres, 114, https://doi.org/10.1029/2008JD010917, _eprint: https://agupubs.onlinelibrary.wiley.com/doi/pdf/10.1029/2008JD010917, 2009.

Jiang, H., Xue, H., Teller, A., Feingold, G., and Levin, Z.: Aerosol effects on the lifetime of shallow cumulus, Geophysical Research Letters, 33, https://doi.org/10.1029/2006GL026024, _eprint: https://agupubs.onlinelibrary.wiley.com/doi/pdf/10.1029/2006GL026024, 2006.

https://doi.org/10.5194/egusphere-2026-3677
Preprint. Discussion started: 10 July 2026

Johnson, R. H. and Lin, X.: Episodic Trade Wind Regimes over the Western Pacific Warm Pool, https://journals.ametsoc.org/view/journals/atsc/54/15/1520-0469_1997_054_2020_etwrot_2.0.co_2.xml, 1997.

Katzwinkel, J., Siebert, H., Heus, T., and Shaw, R. A.: Measurements of Turbulent Mixing and Subsiding Shells in Trade Wind Cumuli, https://doi.org/10.1175/JAS-D-13-0222.1, 2014.

Khain, A., Pokrovsky, A., Pinsky, M., Seifert, A., and Phillips, V.: Simulation of effects of atmospheric aerosols on deep turbulent convective clouds using a spectral microphysics mixed-phase cumulus cloud model. Part I: Model description and possible applications, Journal of the atmospheric sciences, 61, 2963–2982, 2004.

Khain, A., Pinsky, M., Eytan, E., Koren, I., Altaratz, O., Arieli, Y., and Gavze, E.: Dynamics and microphysics in small developing cumulus clouds, Atmospheric Research, 307, 107 454, https://doi.org/10.1016/j.atmosres.2024.107454, 2024.

Khairoutdinov, M.: System for Atmospheric Modeling, http://rossby.msrc.sunysb.edu/~marat/SAM.html.

Khairoutdinov, M. F. and Randall, D. A.: Cloud resolving modeling of the ARM summer 1997 IOP: Model formulation, results, uncertainties, and sensitivities, Journal of Atmospheric Sciences, 60, 607–625, 2003.

Kogan, Y. L.: The simulation of a convective cloud in a 3-D model with explicit microphysics. Part I: Model description and sensitivity experiments, Journal of the Atmospheric Sciences, 48, 1160–1189, 1991.

Kuang, Z. and Bretherton, C. S.: A Mass-Flux Scheme View of a High-Resolution Simulation of a Transition from Shallow to Deep Cumulus Convection, https://doi.org/10.1175/JAS3723.1, 2006.

Laird, N. F.: Humidity Halos Surrounding Small Cumulus Clouds in a Tropical Environment, https://doi.org/10.1175/JAS3538.1, 2005.

Lensky, I. M. and Rosenfeld, D.: The time-space exchangeability of satellite retrieved relations between cloud top temperature and particle effective radius, Atmospheric Chemistry and Physics, 6, 2887–2894, https://doi.org/10.5194/acp-6-2887-2006, 2006.

Lim, J.-S. and Hoffmann, F.: Life Cycle Evolution of Mixing in Shallow Cumulus Clouds, Journal of Geophysical Research: Atmospheres, 129, e2023JD040 393, https://doi.org/10.1029/2023JD040393, _eprint: https://agupubs.onlinelibrary.wiley.com/doi/pdf/10.1029/2023JD040393, 2024.

Lu, M.-L., McClatchey, R. A., and Seinfeld, J. H.: Cloud Halos: Numerical Simulation of Dynamical Structure and Radiative Impact, https://journals.ametsoc.org/view/journals/apme/41/8/1520-0450_2002_041_0832_chnsod_2.0.co_2.xml, 2002.

Lu, M.-L., Wang, J., Flagan, R. C., Seinfeld, J. H., Freedman, A., McClatchey, R. A., and Jonsson, H. H.: Analysis of Humidity Halos around Trade Wind Cumulus Clouds, https://journals.ametsoc.org/view/journals/atsc/60/8/1520-0469_2003_60_1041_aohhat_2.0.co_2.xml, 2003.

Neggers, R. A. J. and Griewank, P. J.: A Binomial Stochastic Framework for Efficiently Modeling Discrete Statistics of Convective Populations, Journal of Advances in Modeling Earth Systems, 13, e2020MS002 229, https://doi.org/10.1029/2020MS002229, _eprint: https://agupubs.onlinelibrary.wiley.com/doi/pdf/10.1029/2020MS002229, 2021.

Perry, K. D. and Hobbs, P. V.: Influences of Isolated Cumulus Clouds on the Humidity of Their Surroundings, https://journals.ametsoc.org/view/journals/atsc/53/1/1520-0469_1996_053_0159_ioicco_2_0_co_2.xml, 1996.

Pinsky, M. and Khain, A.: Analytical Investigation of the Role of Lateral Mixing in the Evolution of Nonprecipitating Cumulus. Part II: Dissolving Stage, https://doi.org/10.1175/JAS-D-19-0118.1, 2020.

Pinsky, M. and Khain, A.: Convective and Turbulent Motions in Nonprecipitating Cu. Part III: Characteristics of Turbulence Motions, https://doi.org/10.1175/JAS-D-21-0223.1, 2023.

Pinsky, M., Eytan, E., Koren, I., Altaratz, O., and Khain, A.: Convective and turbulent motions in nonprecipitating Cu. Part I: Method of separation of convective and turbulent motions, Journal of the Atmospheric Sciences, 78, 2307–2321, 2021.

https://doi.org/10.5194/egusphere-2026-3677
Preprint. Discussion started: 10 July 2026

Quaas, J., Arola, A., Cairns, B., Christensen, M., Deneke, H., Ekman, A. M. L., Feingold, G., Fridlind, A., Gryspeerdt, E., Hasekamp, O., Li, Z., Lipponen, A., Ma, P.-L., Mülmenstädt, J., Nenes, A., Penner, J. E., Rosenfeld, D., Schrödner, R., Sinclair, K., Sourdeval, O., Stier, P., Tesche, M., van Diedenhoven, B., and Wendisch, M.: Constraining the Twomey effect from satellite observations: issues and perspectives, Atmospheric Chemistry and Physics, 20, 15 079–15 099, https://doi.org/10.5194/acp-20-15079-2020, 2020.

Radke, L. F. and Hobbs, P. V.: Humidity and Particle Fields Around Some Small Cumulus Clouds, https://journals.ametsoc.org/view/journals/atsc/48/9/1520-0469_1991_048_1190_hapfas_2_0_co_2.xml, 1991.

Schmeissner, T., Shaw, R. A., Ditas, J., Stratmann, F., Wendisch, M., and Siebert, H.: Turbulent Mixing in Shallow Trade Wind Cumuli: Dependence on Cloud Life Cycle, https://doi.org/10.1175/JAS-D-14-0230.1, 2015.

Scorer, R. S. and Ludlam, F. H.: Bubble theory of penetrative convection, Quarterly Journal of the Royal Meteorological Society, 79, 94–103, https://doi.org/10.1002/qj.49707933908, _eprint: https://rmets.onlinelibrary.wiley.com/doi/pdf/10.1002/qj.49707933908, 1953.

Siebesma, A. P., Bretherton, C. S., Brown, A., Chlond, A., Cuxart, J., Duynkerke, P. G., Jiang, H., Khairoutdinov, M., Lewellen, D., Moeng, C.-H., Sanchez, E., Stevens, B., and Stevens, D. E.: A Large Eddy Simulation Intercomparison Study of Shallow Cumulus Convection, Journal of the Atmospheric Sciences, 60, 1201 – 1219, https://doi.org/10.1175/1520-0469(2003)60<1201:ALESIS>2.0.CO;2, place: Boston MA, USA, 2003.

Stevens, B.: ATMOSPHERIC MOIST CONVECTION, Annual Review of Earth and Planetary Sciences, 33, 605–643, https://doi.org/10.1146/annurev.earth.33.092203.122658, 2005.

Wang, Y. and Geerts, B.: Humidity variations across the edge of trade wind cumuli: Observations and dynamical implications, Atmospheric Research, 97, 144–156, https://doi.org/10.1016/j.atmosres.2010.03.017, 2010.

Witte, M. K., Chuang, P. Y., and Feingold, G.: On clocks and clouds, Atmospheric Chemistry and Physics, 14, 6729–6738, https://doi.org/10.5194/acp-14-6729-2014, 2014.

Zhang, S., Xue, H., and Feingold, G.: Vertical profiles of droplet effective radius in shallow convective clouds, Atmospheric Chemistry and Physics, 11, 4633–4644, https://doi.org/10.5194/acp-11-4633-2011, 2011.

Zhao, M. and Austin, P. H.: Life Cycle of Numerically Simulated Shallow Cumulus Clouds. Part II: Mixing Dynamics, https://doi.org/10.1175/JAS3415.1, 2005a.

Zhao, M. and Austin, P. H.: Life Cycle of Numerically Simulated Shallow Cumulus Clouds. Part I: Transport, https://doi.org/10.1175/JAS3414.1, 2005b.